

UNFITTED NITSCHÉ'S METHOD FOR COMPUTING WAVE MODES IN TOPOLOGICAL MATERIALS

HAILONG GUO*, XU YANG†, AND YI ZHU‡

Abstract. In this paper, we propose an unfitted Nitsche's method for computing wave modes in topological materials. The proposed method is based on Nitsche's technique to study the performance-enhanced topological materials which have strongly heterogeneous structures (*e.g.*, the refractive index is piecewise constant with high contrasts). For periodic bulk materials, we use Floquet-Bloch theory and solve an eigenvalue problem on a torus with unfitted meshes. For the materials with a line defect, a sufficiently large domain with zero boundary conditions is used to compute the localized eigenfunctions corresponding to the edge modes. The interfaces are handled by Nitsche's method on an unfitted uniform mesh. We prove the proposed methods converge optimally, and present numerical examples to validate the theoretical results and demonstrate the capability of simulating topological materials.

AMS subject classifications.

Key words. Nitsche's method, photonic graphene, topological material, edge state

1. Introduction. The past decade has witnessed an explosion of research on topological materials. The delicate structures of these materials admit novel and subtle propagating wave patterns—immune to backscattering from disorder and defects [2, 20, 27, 32, 33]. The underlying mechanism is the existence of so-called “topologically protected edge states”. These wave modes, which propagate along and decay rapidly transverse to the edge, are robust against local defects. Thus they can be used to transfer energy, information and so on. Over the past few years, in addition to the electronic system in which the topological phenomena was firstly studied, such topological phenomena have been experimentally realized in many other physical systems, such as electromagnetic waves in photonic systems, acoustic waves in phononic systems [1, 27, 28, 35, 37, 38].

There are many physical models which admit topologically protected edge states. This work is concerned with edge states in topological photonic materials. The mathematical problem that we study is the following eigenvalue problem

$$\mathcal{L}^W \Psi \equiv -\nabla \cdot W(\mathbf{x}) \nabla \Psi(\mathbf{x}) = E \Psi(\mathbf{x}), \quad \mathbf{x} = (x_1, x_2) \in \mathbb{R}^2. \quad (1.1)$$

This equation arises in the in-plane propagation in a photonic crystal whose permittivity is invariant along the longitudinal direction. In this scenario, the electromagnetic fields $(E_1, E_2, E_3, H_1, H_2, H_3)$ can be divided into two decoupled components, transverse electric (TE) mode (E_1, E_2, H_3) and transverse magnetic (TM) mode (H_1, H_2, E_3) . The admissible TE modes in a specific material, characterized by the material weight function $W(\mathbf{x})$, satisfy the above eigenvalue problem (1.1). Here, $\Psi(\mathbf{x})$ corresponds to the longitudinal magnetic field H_3 and the eigenvalue E equals ω^2 with ω being the frequency of the electromagnetic fields. The other two components of the TE modes are $(E_1, E_2) = \pm \frac{i}{\sqrt{E}} (-\partial_{x_2} \Psi, \partial_{x_1} \Psi)$ corresponding to

*School of Mathematics and Statistics, The University of Melbourne, Parkville, VIC 3010, Australia (hailong.guo@unimelb.edu.au).

†Department of Mathematics, University of California, Santa Barbara, CA, 93106, USA (xuyang@math.ucsb.edu).

‡Zhou Pei-Yuan Center for Applied Mathematics, Tsinghua University, Beijing, 100084, People's Republic of China (yizhu@mail.tsinghua.edu.cn).

frequency $\pm\sqrt{E}$ respectively. We refer to [21] for more details. Though the eigenvalue problem (1.1) can also be obtained in other physical setups such as acoustic waves, we restrict our physical applications in the photonic aspect.

To ensure the existence the topological edge states, delicate structures are required for the material weight $W(\mathbf{x})$. Here we focus on the honeycomb-based material weight. The corresponding material is referred as to “photonic graphene”. Specifically, the material weight is of the form

$$W(\mathbf{x}) = A(\mathbf{x}) + \delta\kappa(\delta\mathbf{k}_2 \cdot \mathbf{x})B(\mathbf{x}), \quad (1.2)$$

where $A(\mathbf{x})$ and $B(\mathbf{x})$ are hexagonally periodic Hermitian matrices, $\kappa(\cdot) \in \mathbb{R}$ is a bounded transition function and $\delta > 0$ is a parameter characterizing the intensity and width of the transition, and the detailed conditions are given in Section 2. From the application point of view, we usually need to understand the bulk property and edge state property. Understanding the bulk property requires that we solve the eigenvalue problem on a torus using the Floquet-Bloch theory. On the other hand, to investigate the edge states, we have to solve the eigenvalue problem in a cylinder since the existence of the transition breaks the periodicity along one direction.

Regarding the analytical understanding of the eigenvalue problem (1.1) with the material weight (1.2), Lee-Thorp *et al.* proved that the perfect honeycomb material weight ensures the existence of Dirac points in the spectrum, which can be used to construct topological edge states [21]. They also perturbatively constructed the edge states for specific parallel wavenumbers when δ is small and the material weight $W(\mathbf{x})$ is smooth. Their work greatly extends our knowledge on the understanding of topological edge states in a photonic system. However, their results are mostly on the existence aspect and lack the global structure of the bulk dispersion relation and edge states. All of these important studies rely on numerical simulations.

Due to the particular structure of the photonic crystals, spectral method and finite element method are the two most popular methods. The spectral method utilizes the periodicity of the coefficients and eigenfunctions. Expanding the coefficients and Bloch modes into Fourier series and truncating the series into finite terms, the spectral method can achieve an exponential accuracy for smooth coefficients. It is widely used for computing Bloch modes and corresponding energy surfaces [34, 36]. However, one of the main shortcomings is that the final matrix is usually not sparse. If the material weight varies drastically or contain discontinuities, this method requires a large number of Fourier modes to resolve the coefficients, thus the computation becomes expensive to solve the numerical algebra associated with a large and dense matrix.

A competitive alternative is the finite element method. In fact, finite element methods have been adopted in the computation of topological edge modes. In our recent work [14], we proposed a superconvergent post-processing method to compute topological edge modes for photonic graphene with smooth weight coefficient. The key idea is to recover more accurate gradients for numerical eigenfunctions and improve the accuracy of eigenvalues by using Rayleigh quotient. The superconvergent recovered gradient also enables us to reconstruct the full electromagnetic fields in real applications. Due to the high contrast nature of the material coefficient, the proposed method can not be generalized directly. The main difficulties are caused by the heterogeneous structure. The existing of the jump in the material weights W implies the non-smoothness of eigenfunctions at the material interfaces. Although the classical finite element methods will work if the underlying mesh is fitted to the interface [4, 8, 11], it is in general time-consuming and nontrivial to generate a body-fitted mesh. The drawbacks become more serious for the interface with complicated

geometric structure. For the honeycomb structure, the discontinuities in the material weight function is copied periodically, which makes the generation of body-fitted meshes become challenging. Furthermore, the unstructured nature of the body-fitted meshes will introduce additional difficulties to impose the periodical or Bloch period boundary condition. Those difficulties can be alleviated by adopting the unfitted numerical methods where the underlying meshes are independent of the location of the material interface. To handle the non-smoothness across the material over the interface, one may need modify the finite difference stencil [22, 24, 30, 31], finite element basis functions [10, 13, 17, 18, 23, 25, 26], or the weak formulation [3, 7, 12, 16].

The main purpose of the paper is to propose a new kind of unfitted Nitsche's method based on the Floquet-Bloch transformation for computing dispersive relation and topological edge modes in a honeycomb structure with strong heterogeneities. The unfitted Nitsche's method was originally proposed in [16] for the elliptic interface problem with real coefficients. The key idea is to construct the approximation on each fictitious domain induced by the material interfaces and couple them together by the Nitsche's technique [29]. For the development and application of the unfitted Nitsche's method, the interesting readers are referred to the recent review paper [7]. Compared to the existing unfitted Nitsche's methods [3, 7, 16], the proposed unfitted Nitsche's method uses Floquet-Bloch theory and solves an eigenvalue problem on a torus. For the \mathcal{C} -symmetry breaking case where the eigenvalue problem contains complex matrix-valued coefficients, a sufficiently large domain with zero boundary conditions is used to compute the localized eigenfunctions (edge mode).

One of the difficulties in analyzing the stability of the discrete Nitsche's bilinear form is that it involves the solution itself in addition to its gradient. To the best of our knowledge, the existing unfitted Nitsche's method only focuses on the pure diffusion equation. To establish the stability, we need the trace theorem on cut elements, i.e. elements cut by the interface. The existing trace [7, 16] theorem for the cut element involves both parts of the cut element. Direct application of the theorem is not able to entitle us the full possibility to prove the coercivity of the Nitsche's bilinear form. Therefore, we build up a new trace inequality which involves one part of the cut element. The new trace inequality enables us to establish the stability and continuity for Nitsche's bilinear form in term of the energy norm. Using the approximation theory of the compact operator [5] and the interpolation error estimates, we are able to show the optimal convergence results for both eigenvalue and eigenfunction approximation by the proposed unfitted Nitsche's method. In particular, the established error estimate is independent of the location of the interface and uniform to the jump ratio of the material weight. Furthermore, we show that there is no pollution in the numerical spectrum.

The rest of the paper is organized as follows. In Section 2, we present the physical background of photonic graphene and mathematical setup. In Section 3, we focus on the computation of dispersive relation. We start the section by the formulation of the unfitted Nitsche's method on the torus. The stability and continuity of the unfitted Nitsche's weak formulation are established. Then, we extend the unfitted Nitsche's to compute topological edge modes in a cylinder domain. In Section 4, we prove the numerically approximated eigenpair converges optimally to the exact eigenpair. In Section 5, we present several numerical examples to confirm the theoretical results. We make conclusive remarks in Section 6.

2. Physical problems and preliminaries. We will focus on the honeycomb-based photonic materials, and present the physical setup and briefly review the un-

derlying theory.

2.1. honeycomb structured material weight. We consider the following specific hexagonal lattice

$$\Lambda = \mathbb{Z}\mathbf{v}_1 + \mathbb{Z}\mathbf{v}_2 = \{m_1\mathbf{v}_1 + m_2\mathbf{v}_2 : m_1, m_2 \in \mathbb{Z}\}, \quad (2.1)$$

with the lattice basis vectors

$$\mathbf{v}_1 = \begin{pmatrix} \frac{\sqrt{3}}{2} \\ \frac{1}{2} \end{pmatrix}, \quad \mathbf{v}_2 = \begin{pmatrix} \frac{\sqrt{3}}{2} \\ -\frac{1}{2} \end{pmatrix}.$$

The fundamental cell is chosen to be the parallelogram:

$$\Omega = \{\theta_1\mathbf{v}_1 + \theta_2\mathbf{v}_2 : 0 \leq \theta_j \leq 1, j = 1, 2\}, \quad (2.2)$$

with $|\Omega|$ standing for the area of Ω .

The dual lattice

$$\Lambda^* = \{m_1\mathbf{k}_1 + m_2\mathbf{k}_2 := (m_1, m_2) \in \mathbb{Z}^2\} = \mathbb{Z}\mathbf{k}_1 \oplus \mathbb{Z}\mathbf{k}_2, \quad (2.3)$$

is generated by the dual lattice vectors $\mathbf{k}_1, \mathbf{k}_2$ which satisfy $\mathbf{k}_i \cdot \mathbf{v}_j = 2\pi\delta_{ij}$, ($i, j = 1, 2$). Specifically, the dual lattice vectors are

$$\mathbf{k}_1 = \frac{4\sqrt{3}}{3} \begin{pmatrix} \frac{1}{2} \\ \frac{\sqrt{3}}{2} \end{pmatrix}, \quad \mathbf{k}_2 = \frac{4\sqrt{3}}{3} \begin{pmatrix} \frac{1}{2} \\ -\frac{\sqrt{3}}{2} \end{pmatrix}. \quad (2.4)$$

Throughout this work, we choose the parallelogram Ω^* :

$$\Omega^* = \{\theta_1\mathbf{k}_1 + \theta_2\mathbf{k}_2 : -\frac{1}{2} \leq \theta_j \leq \frac{1}{2}, j = 1, 2\}, \quad (2.5)$$

as the fundamental dual cell.

Let $\mathbf{A} = \frac{1}{3}(\mathbf{v}_1 + \mathbf{v}_2) \in \Omega, \mathbf{B} = \frac{2}{3}(\mathbf{v}_1 + \mathbf{v}_2) \in \Omega$. Define the honeycomb lattice $\Lambda_h = (\mathbf{A} + \Lambda) \cup (\mathbf{B} + \Lambda)$. Note that Λ_h is not a Bravais lattice since it has two sites per unit cell.

Let $B_r(\mathbf{x}_0)$ be the ball centered at \mathbf{x}_0 with the radius r . Throughout this work, we require that $r < \frac{1}{2}|\mathbf{A} - \mathbf{B}|$ which implies that $B_r(\mathbf{A})$ and $B_r(\mathbf{B})$ are disjoint. We divide the fundamental cell into two parts, $\Omega_1 = B_r(\mathbf{A}) \cup B_r(\mathbf{B})$ and $\Omega_2 = \Omega/\Omega_1$. Define the piece-wise honeycomb function

$$\epsilon(\mathbf{x}) = \begin{cases} C_{\mathbf{A}}, & \text{if } \mathbf{x} \in B_r(\mathbf{A}) + \Lambda \\ C_{\mathbf{B}}, & \text{if } \mathbf{x} \in B_r(\mathbf{B}) + \Lambda \\ C_0, & \text{if } \mathbf{x} \in \Omega_2 + \Lambda \end{cases}, \quad (2.6)$$

where $C_j, j = \mathbf{A}, \mathbf{B}, 0$ are positive constants. C_0 is regarded as the value of the background and $C_{\mathbf{A}}, C_{\mathbf{B}}$ are the values against the background. It is obvious that $\epsilon(\mathbf{x})$ is Λ -periodic, i.e., $\epsilon(\mathbf{x} + \mathbf{v}) = \epsilon(\mathbf{x})$ for all $\mathbf{v} \in \Lambda$.

In this work, we use the following material weight as our prototype

$$W(\mathbf{x}) = \begin{pmatrix} \epsilon(\mathbf{x}) & i\gamma \\ -i\gamma & \epsilon(\mathbf{x}) \end{pmatrix}^{-1}. \quad (2.7)$$

This material weight corresponds to the magneto-optical material [15]. $\gamma \in \mathbb{R}$ is called Faraday-rotation constant satisfying $\min(\epsilon(\mathbf{x})^2 - \gamma^2) > c_0 > 0$, which ensures $W(\mathbf{x})$ is uniformly elliptic. In real materials, the strength of the Faraday-rotation is much smaller than the permittivity ϵ , hence

$$W(\mathbf{x}) \approx \epsilon(\mathbf{x})^{-1}I + \gamma\epsilon^{-2}\sigma_2, \quad (2.8)$$

where $\sigma_2 = \begin{pmatrix} 0 & -i \\ i & 0 \end{pmatrix}$ is a Pauli matrix.

2.2. Eigenvalue problem in a torus. Consider the material weight of the form (2.7) or (2.8). $W(\mathbf{x})$ is Λ -periodic when γ is constant. We can restrict our analysis in a torus by Floquet-Bloch theory. Before proceeding further, we introduce the following function space

$$\begin{aligned} L_{per}^2(\Lambda) &= \{f(\mathbf{x}) \in L_{loc}^2(\mathbb{R}^2, \mathbb{C}) : f(\mathbf{x} + \mathbf{v}) = f(\mathbf{x}), \forall \mathbf{v} \in \Lambda, \mathbf{x} \in \mathbb{R}^2\} \\ L_{\mathbf{k}}^2(\Lambda) &= \{g(\mathbf{x}) : e^{-i\mathbf{k}\cdot\mathbf{x}}g(\mathbf{x}) \in L_{per}^2(\Lambda)\}. \end{aligned}$$

Note that functions in $L_{\mathbf{k}}^2(\Lambda)$ are quasi-periodic. Namely, if $g(\mathbf{x}) \in L_{\mathbf{k}}^2(\Lambda)$, then $g(\mathbf{x} + \mathbf{v}) = e^{i\mathbf{k}\cdot\mathbf{v}}g(\mathbf{x}), \forall \mathbf{v} \in \Lambda$. Similarly, we can also define $H_{per}^s(\Lambda)$ and $H_{\mathbf{k}}(\Lambda)$ in a standard way.

According to Floquet-Bloch theory, the spectrum of \mathcal{L}^W in $L^2(\mathbb{R}^2)$ can be represented by the spectrum \mathcal{L}^W in $L_{\mathbf{k}}^2(\Lambda)$. Namely, we solve the following $L_{\mathbf{k}}^2(\Lambda)$ -eigenvalue problem

$$\mathcal{L}^W \Phi(\mathbf{x}) = E\Phi(\mathbf{x}), \quad \Phi(\mathbf{x}) \in L_{\mathbf{k}}^2(\Lambda). \quad (2.9)$$

Due to the periodicity, we can restrict \mathbf{k} in the fundamental dual cell Ω^* . For a fixed $\mathbf{k} \in \Omega^*$, there exists a sequence of pairs $(E_m(\mathbf{k}), \Phi_m(\mathbf{x}; \mathbf{k})), m = 1, 2, \dots$ satisfying the above eigenvalue problem. Here $E_m(\mathbf{k}), m = 1, 2, \dots$ are called dispersion band functions which have been ordered as $0 < E_1(\mathbf{k}) \leq E_2(\mathbf{k}) \leq E_3(\mathbf{k}) \leq \dots$. The corresponding eigenfunctions $\Phi_m(\mathbf{x}; \mathbf{k})$ are referred as the Bloch waves. Moreover, the set $\{\Phi_m(\mathbf{x}; \mathbf{k}), m \in \mathbb{N}, \mathbf{k} \in \Omega^*\}$ forms a ‘‘generalized’’ basis of $L^2(\mathbb{R}^2)$ and the spectrum of \mathcal{L}^W in $L^2(\mathbb{R}^2)$, $\sigma(\mathcal{L}^W)$ coincides with the Bloch spectrum, the union of the images of all the mappings $E_m(\mathbf{k})$, i.e.,

$$\sigma(\mathcal{L}^W) = \bigcup_{m=1}^{\infty} \left[\inf_{\mathbf{k} \in \Omega^*} E_m(\mathbf{k}), \sup_{\mathbf{k} \in \Omega^*} E_m(\mathbf{k}) \right]. \quad (2.10)$$

Generally, it is impossible to solve the eigenvalue problem (2.9) analytically. A natural numerical scheme is the spectral method. Namely, we can expand $W(\mathbf{x})$ and $\Phi(\mathbf{x})$ into their Fourier series. By truncating the series into finite terms, we can easily solve the reduced eigenvalue problem for a matrix. If $W(\mathbf{x})$ is smooth, by Lax-Milgram theorem, $\Phi(\mathbf{x})$ is also smooth. We only need a few terms to approximate $W(\mathbf{x})$ and $\phi(\mathbf{x})$ due to the exponential accuracy. The shortcoming of this method is that the reduced matrix is not sparse. When we need a large number of terms to approximate $W(\mathbf{x})$, this method becomes costly, for example, $W(\mathbf{x})$ changes greatly or is even discontinuous.

If $\gamma = 0$, $W(\mathbf{x})$ is a honeycomb structured material defined in [21], i.e., $W(\mathbf{x})$ is even, real and $\frac{2\pi}{3}$ -rotation invariant. According to [21], there generically exist the so-called Dirac points—conical singularities in the dispersion band functions $E_m(\mathbf{k})$ at $\mathbf{k} = \mathbf{K}, \mathbf{K}'$ for some m . If $\gamma \neq 0$ but is still a constant, the material weight $W(\mathbf{x})$ is now complex, local spectral gaps open near the Dirac points due to the complex-conjugate symmetry breaking.

2.3. Honeycomb structured material weight with a line defect. Dirac points provide a mechanism to generate the so-called topological edge states via introducing a line defect. Define a transition function (referred as to domain wall function) $\kappa(\zeta) \in L^\infty(\mathbb{R}, \mathbb{R})$ with $\kappa(\pm\infty) = \pm\kappa_\infty$. Without loss of generality, we require that $\kappa_\infty > 0$. A typical example of this transition function is the step function

$$\kappa(\zeta) = \begin{cases} -\kappa_\infty, & \zeta < 0, \\ 0, & \zeta = 0, \\ +\kappa_\infty, & \zeta > 0. \end{cases} \quad (2.11)$$

A typical smooth transition function is $\kappa(\zeta) = \kappa_\infty \tanh(\zeta)$.

A line defect is introduced if we choose the Faradi-rotation γ in (2.7) to be a transition function along a direction. Namely $\gamma = \kappa(\mathbf{n} \cdot \mathbf{x})$ where $\mathbf{n} \neq 0$ is the normal direction of the line defect. Obviously, if $\kappa(\zeta)$ is the step function (2.11), the line $\mathbf{n}^\perp \mathbb{R}$ is the interface of two different materials (we also call it an edge). In this work we take Zigzag edge as our prototype. In this case, $\mathbf{n} = \mathbf{k}_2$ and the line $\mathbf{v}_1 \mathbb{R}$ is the edge. Note that $W(\mathbf{x})$ is periodic along \mathbf{v}_1 direction but loses the periodicity along \mathbf{v}_2 direction.

Let $\Sigma = \mathbb{R}^2 / \mathbb{Z}\mathbf{v}_1$ be a cylinder. The fundamental domain for Σ is $\Omega_\Sigma \equiv \{\tau_1 \mathbf{v}_1 + \tau_2 \mathbf{v}_2 : 0 \leq \tau_1 \leq 1, \tau_2 \in \mathbb{R}\}$. Define the function spaces

$$\begin{aligned} L_{per}^2(\Sigma) &= \{f(\mathbf{x}) \in L^2(\Omega_\Sigma, \mathbb{C}) : f(\mathbf{x} + \mathbf{v}_1) = f(\mathbf{x})\} \\ L_{k_\parallel}^2(\Sigma) &= \{g(\mathbf{x}) \in L^2(\Omega_\Sigma, \mathbb{C}) : g(\mathbf{x} + \mathbf{v}_1) = e^{ik_\parallel} g(\mathbf{x})\}. \end{aligned}$$

We solve the eigenvalue problem (1.1) in $L_{k_\parallel}^2(\Sigma)$. For a given $k_\parallel \in [0, 2\pi]$, the continuous spectrum of \mathcal{L}^W can be obtained by letting $\mathbf{k}_2 \cdot \mathbf{x}$ tend to $\pm\infty$. Indeed,

$$\sigma_{c, k_\parallel}(\mathcal{L}^W) = \bigcup_{m=1}^{\infty} \left[\inf_{\lambda \in [-1/2, 1/2]} E_m(\lambda \mathbf{k}_2 + \frac{1}{2\pi} k_\parallel \mathbf{k}_1), \sup_{\lambda \in [-1/2, 1/2]} E_m(\lambda \mathbf{k}_2 + \frac{1}{2\pi} k_\parallel \mathbf{k}_1) \right] \quad (2.12)$$

Due to the subtle symmetries of the setup, there exists point spectrum and the corresponding eigenfunctions are referred as to edge states. Namely, $\Psi(\mathbf{x})$ satisfies

$$\mathcal{L}^W \Psi(\mathbf{x}; k_\parallel) = E(k_\parallel) \Psi(\mathbf{x}; k_\parallel), \quad (2.13)$$

$$\Psi(\mathbf{x} + \mathbf{v}_1; k_\parallel) = e^{ik_\parallel} \Psi(\mathbf{x}; k_\parallel), \quad (2.14)$$

$$\Psi(\mathbf{x}; k_\parallel) \rightarrow 0 \quad \text{as } |\mathbf{x} \cdot \mathbf{k}_2| \rightarrow \infty. \quad (2.15)$$

3. Unfitted Nitsche's method. In this section, we propose the Floquet-Bloch theory based unfitted Nitsche's methods for simulation topological materials. Firstly, we focus on the computing dispersive relation. Then, we put our extend the method to computing edge states.

3.1. Unfitted Nitsche's method for computing dispersive relation. In this section, we are interested in the efficient numerical solution of the eigenvalue problem (2.9) in a torus. One of the main numerical difficulties is the existence of the high contrast in the material weight $W(\mathbf{x})$, which may lower the regularity of eigenfunctions. To model the discontinuity, we use the interface conditions as [24] and the $L_{\mathbf{k}}^2(\Lambda)$ -eigenvalue problem (2.9) can be converted into the following interface

$L_{\mathbf{k}}^2(\Lambda)$ -eigenvalue problem

$$\mathcal{L}^W \Phi(\mathbf{x}) = E\Phi(\mathbf{x}), \quad (3.1)$$

$$\llbracket \Psi \rrbracket = \left[\left[W \frac{\partial \Psi}{\partial n} \right] \right] = 0, \quad \text{on } \Gamma; \quad (3.2)$$

where $\Phi(\mathbf{x}) \in L_{\mathbf{k}}^2(\Lambda)$, $\llbracket v \rrbracket$ is the jump in value of a function v crossing the interface Γ , and n is the unit outer normal vector of Γ .

To deal with quasi-periodicity of functions in $L_{\mathbf{k}}^2(\Lambda)$, we apply the Floquet-Bloch transform $\Phi(\mathbf{x}; \mathbf{k}) = e^{i\mathbf{k}\cdot\mathbf{x}}\phi(\mathbf{x}; \mathbf{k})$. We transfer the eigenvalue problem (3.1) to the following interface $L_{per}^2(\Lambda)$ -eigenvalue problem

$$\mathcal{L}^W(\mathbf{k})\phi(\mathbf{x}) = E(\mathbf{k})\phi(\mathbf{x}), \quad (3.3)$$

$$\llbracket \phi \rrbracket = \llbracket W(\nabla + i\mathbf{k})\phi \cdot n \rrbracket = 0, \quad \text{on } \Gamma; \quad (3.4)$$

where $\phi(\mathbf{x}) \in L_{per}^2(\Lambda)$ and

$$\mathcal{L}^W(\mathbf{k}) = (\nabla + i\mathbf{k}) \cdot W(\mathbf{x})(\nabla + i\mathbf{k}). \quad (3.5)$$

To address the numerical challenge brought by the interface condition (3.4), the most straightforward idea is to use finite element methods with body-fitted meshes [4, 8], i.e. use meshes to resolve the discontinuity. But this brings two new *difficulties*: firstly, the body-fitted meshes, in general, are unstructured meshes on which it is difficult to impose the periodic boundary conditions; secondly, it is technically hard to generate body-fitted meshes, in special for topological materials with complicated geometric structures. In this paper, we avoid those two difficulties by introducing the unfitted Nitsche's methods [7, 16].

3.1.1. Unfitted Nitsche's method in a torus. In this part, we introduce the unfitted Nitsche's method for the interface $L_{per}^2(\Lambda)$ -eigenvalue problem (3.3)–(3.4). To avoid generating of body-fitted meshes for complicate topological structure and simply the imposing of periodical boundary condition, we take the uniform triangulation of Ω . The uniform triangulation is obtained by dividing Ω into N^2 sub-rhombuses with mesh size $h = \frac{\|\mathbf{v}_1\|_2}{N}$ and then splitting each sub-rhomb into two isosceles triangles. In addition, we assume that N is sufficiently large such that the following assumption holds:

ASSUMPTION 3.1. *The interface Γ intersects each interface element boundary ∂K exactly twice, and each open edge at most once.*

The elements of \mathcal{T}_h are categorized into two different classes: regular elements and interface elements. An element τ is called an interface element if the interface Γ passes through \bar{K} . The set of all elements that intersect the interface Γ is denoted by $\mathcal{T}_{\Gamma,h}$. Then, it is easy to see that

$$\mathcal{T}_{\Gamma,h} = \{K \in \mathcal{T}_h : \Gamma \cap \bar{K} \neq \emptyset\}, \quad (3.6)$$

and denote the union of all such type elements by

$$\Omega_{\Gamma,h} = \bigcup_{K \in \mathcal{T}_{\Gamma,h}} K. \quad (3.7)$$

Denote the set of all elements covering subdomain Ω_i to be

$$\mathcal{T}_{i,h} = \{K \in \mathcal{T}_h : \bar{\Omega}_i \cap \bar{K} \neq \emptyset\}, \quad i = 1, 2; \quad (3.8)$$

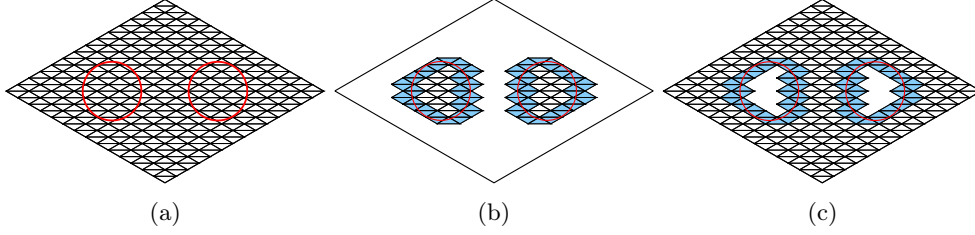


Fig. 3.1: Triangulation \mathcal{T}_h on fundamental cell. (a): Triangulation \mathcal{T}_h ; (b): Triangulation $\mathcal{T}_{1,h}$; (c): Triangulation $\mathcal{T}_{2,h}$.

and let

$$\Omega_{i,h} = \bigcup_{K \in \mathcal{T}_{i,h}} K, \quad \omega_{i,h} = \bigcup_{K \in \mathcal{T}_{i,h} \setminus \mathcal{T}_{\Gamma,h}} K, \quad i = 1, 2. \quad (3.9)$$

Figure 3.1 gives an illustration of $\Omega_{i,h}$ and $\omega_{i,h}$. We remark that $\Omega_{1,h}$ and $\Omega_{2,h}$ overlap on $\Omega_{\Gamma,h}$, which is shown as the blue part in Figures 3.1b and 3.1c.

One of main ingredients of unfitted Nitsche's method is to define the finite element space as the direct sum of standard linear finite element spaces on $\Omega_{i,h}$. For such a purpose, we let $V_{i,h}$ be the standard continuous linear finite element space on $\Omega_{i,h}$, i.e.

$$V_{i,h} = \{v \in C^0(\Omega_{i,h}) : v|_K \in \mathbb{P}_1(K) \text{ for any } K \in \mathcal{T}_{i,h}\}, \quad i = 1, 2, \quad (3.10)$$

where $\mathbb{P}_k(K)$ is the space of polynomials with degree less than or equal to k on the element K . The finite element space for the unfitted Nitsche's is defined as $V_h = V_{1,h} \oplus V_{2,h}$. In other words,

$$V_h = \{v_h = (v_{1,h}, v_{2,h}) : v_{i,h} \in V_{i,h}, i = 1, 2\}. \quad (3.11)$$

To impose the periodical boundary condition, we introduce $V_{h,per}$ as a subspace of V_h which is defined as

$$V_{h,per} = \{v_h \in V_h : v_h(\mathbf{x} + \mathbf{v}) = v_h(\mathbf{x}), \forall \mathbf{v} \in \Lambda, \mathbf{x} \in \mathbb{R}^2\}. \quad (3.12)$$

Note that a function in V_h (or $V_{h,per}$) is a vector-valued function from $\mathbb{R}^2 \mapsto \mathbb{R}^2$, which has a zero component in $\omega_{1,h} \cup \omega_{2,h}$ but in general two non-zero components in $\mathcal{T}_{\Gamma,h}$. It means that one will have two sets of basis functions for any element K in $\mathcal{T}_{\Gamma,h}$: one for $V_{1,h}$ and the other for $V_{2,h}$.

For any interface element K in $\mathcal{T}_{\Gamma,h}$, let $K_i = K \cap \Omega_i$ be the part of K in Ω_i , where $|K_i|$ is the area of K_i . Similarly, let $\Gamma_K = \Gamma \cap K$ be the part of Γ in K , where $|\Gamma_K|$ is the measure of Γ_K in \mathbb{R}^1 . Different from the interface elliptic problem considered unfitted Nitsche's method [12, 16], the diffusion coefficient $W(\mathbf{x})$ is complex and matrix-valued. To increase the robustness of the Nitsche's method, we introduce two weights using the maximal norm of W inspired by [3]

$$\kappa_1|_K = \frac{\|W_2\|_\infty |K_1|}{\|W_2\|_\infty |K_1| + \|W_1\|_\infty |K_2|}, \quad \kappa_2|_K = \frac{\|W_1\|_\infty |K_2|}{\|W_2\|_\infty |K_1| + \|W_1\|_\infty |K_2|}, \quad (3.13)$$

which satisfies that $\kappa_1 + \kappa_2 = 1$. Then, we define the weighted averaging of a function v_h on the interface Γ as

$$\{\{v_h\}\} = \kappa_1 v_{1,h} + \kappa_2 v_{2,h}, \quad \{\{v_h\}\}^* = \kappa_2 v_{1,h} + \kappa_1 v_{2,h}. \quad (3.14)$$

Furthermore, we define the constant λ_T as

$$\lambda_K = \frac{h \|W_1\|_\infty \|W_2\|_\infty |\Gamma_K|}{\|W_2\|_\infty |K_1| + \|W_1\|_\infty |K_2|}.$$

It is easy to see that $\lambda_K \leq \|W\|_\infty := \max(\|W_1\|_\infty, \|W_2\|_\infty)$.

The unfitted Nitsche's for the interface $L^2_{per}(\Lambda)$ -eigenvalue problem (3.3)–(3.4) is to find the the eigenpair $(\phi_h, E_h(\mathbf{k})) \in V_{h,per} \times \mathbb{R}$ with $\phi_h \neq 0$ such that

$$a_h(\phi_h, q_h) = E_h(\mathbf{k}) b(\phi_h, q_h), \quad \forall q_h \in V_{h,per}, \quad (3.15)$$

where

$$\begin{aligned} a_h(\phi_h, q_h) &= \sum_{i=1}^2 \int_{\Omega_i} W(\nabla + i\mathbf{k}) \phi_h \cdot \overline{(\nabla + i\mathbf{k}) q_h} d\mathbf{x} - \int_{\Gamma} \{\{W(\nabla + i\mathbf{k}) \phi_h \cdot n\}\} [\overline{q_h}] ds - \\ &\int_{\Gamma} \{\{\overline{W(\nabla + i\mathbf{k}) q_h \cdot n}\}\} [\phi_h] ds + \frac{\lambda}{h} \int_{\Gamma} [\phi_h] [\overline{q_h}] ds, \end{aligned} \quad (3.16)$$

and

$$b(\phi_h, q_h) = \int_{\Omega} \phi_h \cdot \overline{q_h} d\mathbf{x}. \quad (3.17)$$

Here h is the mesh size and λ is a positive parameter. The weak formulation (3.15) is referred to the Nitsche's weak formulation.

3.1.2. Well-posedness of the unfitted Nitsche's method in a torus.

In this part, we shall show the unfitted Nitsche's method is well-posed. We start by showing the following consistency result:

LEMMA 3.2. *Let (ϕ, E) be the eigenpair of the interface $L^2_{per}(\Lambda)$ -eigenvalue problem (3.3)–(3.4). Then (ϕ, E) satisfies*

$$a_h(\phi, q) = E(\mathbf{k}) b(\phi, q), \quad \forall q \in H^1_{per}, \quad (3.18)$$

Proof. For any $\phi, q \in H^1_{per}$, We notice that $[\phi] = [q] = 0$ and hence $a_h(\cdot, \cdot)$ reduces to the standard bilinear formulation. Then (3.18) follows by using the Green's formula on each subdomain Ω_i and the interface condition (3.4). \square

Based on the above Lemma, we can easily deduce following corollary which is known as the Galerkin orthogonality:

COROLLARY 3.3. *Let $(\phi, E(\mathbf{k}))$ be the eigenpair of the interface $L^2_{per}(\Lambda)$ -eigenvalue problem (3.3)–(3.4) and $(\phi_h, E_h(\mathbf{k}))$ be the corresponding approximate eigenpair by the unfitted Nitsche's method. Then we have*

$$a_h(\phi - \phi_h, q_h) = 0, \quad \forall q_h \in V_h. \quad (3.19)$$

To analyze the stability of the bilinear form $a_h(\cdot, \cdot)$, we introduce the following mesh-dependent norm [7, 16]

$$|||\phi|||_h^2 = \|(\nabla + \mathbf{i}\mathbf{k})\phi\|_{0, \Omega_1 \cup \Omega_2}^2 + \sum_{K \in \mathcal{T}_{\Gamma, h}} h^{-1} \|[\![\phi]\!] \|_{0, \Gamma_K}^2. \quad (3.20)$$

We prepare our proof for the stability of the bilinear form by establishing the following Lemma, whose proof is given in Appendix A.

LEMMA 3.4. *Let ϕ_h be a finite element function in V_h . Then the following inequalities hold:*

$$\|\phi_{i,h}\|_{0, \Gamma_K} \leq \frac{4h|\Gamma_K|}{|K_i|} \|\nabla \phi_{i,h}\|_{0, K_i}, \quad (3.21)$$

$$\|\nabla \phi_{i,h}\|_{0, \Gamma_K} \leq \frac{4|\Gamma_K|}{|K_i|} \|\nabla \phi_{i,h}\|_{0, K_i}. \quad (3.22)$$

REMARK 3.1. *The inequality of (3.21) is a refinement of the trace inequality on a cut element in [16]. It is the key to show the stability of the bilinear form.*

Based on the above Lemma, we establish the following error estimates for the weighted averaging

LEMMA 3.5. *Let q_h be a finite element function in V_h . Then the following inequalities hold:*

$$\| \{ \{ (W\mathbf{k}q) \cdot \mathbf{n} \} \} \|_{0, \Gamma_K} \leq 8\lambda_K |\mathbf{k}| \|\nabla q_h\|_{0, K_1 \cup K_2}, \quad (3.23)$$

$$\| \{ \{ (W\nabla q) \cdot \mathbf{n} \} \} \|_{0, \Gamma_K} \leq 8h^{-1} \lambda_K \|\nabla q_h\|_{0, K_1 \cup K_2}. \quad (3.24)$$

Proof. First, we show the inequality (3.23). Using (3.13) and (3.14), we can deduce from Lemma 3.4 that

$$\begin{aligned} \| \{ \{ (W\mathbf{k}q) \cdot \mathbf{n} \} \} \|_{0, \Gamma_K} &= \| \kappa_1 (W_1 \mathbf{k} q_{1,h}) \cdot \mathbf{n} + \kappa_2 (W_2 \mathbf{k} q_{2,h}) \cdot \mathbf{n} \|_{0, \Gamma_K} \\ &\leq \kappa_1 |\mathbf{k}| \|W_1\|_{\infty} \|q_{1,h}\|_{0, \Gamma_K} + \kappa_2 |\mathbf{k}| \|W_2\|_{\infty} \|q_{2,h}\|_{0, \Gamma_K} \\ &= 4\lambda_K |\mathbf{k}| (\|\nabla q_{1,h}\|_{0, K_1} + \|\nabla q_{2,h}\|_{0, K_2}) \\ &\leq 8\lambda_K |\mathbf{k}| \|\nabla q_h\|_{0, K_1 \cup K_2}. \end{aligned} \quad (3.25)$$

The inequality (3.24) is obtained by a similar argument. \square

Now, we are ready to show that the bilinear form $a_h(\cdot, \cdot)$ is coercive and continuous with respect to the above mesh-dependent norm in the following sense

THEOREM 3.6. *Suppose that the stability parameter λ is large enough. Then there exist two constants C_1 and C_2 such that*

$$C_1 |||q_h|||_h^2 \leq a_h(q_h, q_h), \quad \forall q_h \in V_h; \quad (3.26)$$

$$a_h(q_h, \chi_h) \leq C_2 |||q_h|||_h |||\chi_h|||_h, \quad \forall q_h, \chi_h \in V_h. \quad (3.27)$$

Proof. It is noted that (3.27) is a direct consequence of Lemma 3.5. So we only need to justify the inequality (3.26). Letting $\phi_h = q_h$ in (3.16) and applying the

Cauchy-Scharwz inequality and the Young's inequality with ϵ , we have

$$\begin{aligned}
& a_h(q_h, q_h) \\
&= \sum_{i=1}^2 \int_{\Omega_i} W(\nabla + \mathbf{i}\mathbf{k})q_h \cdot \overline{(\nabla + \mathbf{i}\mathbf{k})q_h} dx - \\
& \quad 2\text{Re} \int_{\Gamma} \{W(\nabla + \mathbf{i}\mathbf{k})q_h \cdot \mathbf{n}\} \overline{\{q_h\}} ds + \frac{\lambda}{h} \|\llbracket q_h \rrbracket\|_{0,\Gamma}^2 \\
&\geq C_u \|(\nabla + \mathbf{i}\mathbf{k})q_h\|_{0,\Omega_1 \cup \Omega_2}^2 - 2\|\{W(\nabla + \mathbf{i}\mathbf{k})q_h \cdot \mathbf{n}\}\|_{0,\Gamma} \|\overline{\{q_h\}}\|_{0,\Gamma} + \frac{\lambda}{h} \|\llbracket q_h \rrbracket\|_{0,\Gamma}^2 \\
&\geq C_u \|(\nabla + \mathbf{i}\mathbf{k})q_h\|_{0,\Omega_1 \cup \Omega_2}^2 - \frac{h}{\epsilon} \|\{W(\nabla + \mathbf{i}\mathbf{k})q_h \cdot \mathbf{n}\}\|_{0,\Gamma}^2 + \frac{\lambda - 2\epsilon}{h} \|\llbracket q_h \rrbracket\|_{0,\Gamma}^2 \\
&\geq C_u \|(\nabla + \mathbf{i}\mathbf{k})q_h\|_{0,\Omega_1 \cup \Omega_2}^2 - \frac{h}{\epsilon} \|\{(W\nabla q_h) \cdot \mathbf{n}\}\|_{0,\Gamma}^2 - \\
& \quad \frac{h}{\epsilon} |\mathbf{k}| \|\{(W\mathbf{k}q_h) \cdot \mathbf{n}\}\|_{0,\Gamma}^2 + \frac{\lambda - 2\epsilon}{h} \|\llbracket q_h \rrbracket\|_{0,\Gamma}^2.
\end{aligned}$$

Then, using Lemma 3.5, we can deduce that

$$\begin{aligned}
& a_h(q_h, q_h) \\
&\geq C_u \|(\nabla + \mathbf{i}\mathbf{k})q_h\|_{0,\Omega_1 \cup \Omega_2}^2 - \frac{320}{\epsilon} \|W\|_{\infty} \|\nabla q_h\|_{0,\Omega_1 \cup \Omega_2}^2 + \frac{\lambda - 2\epsilon}{h} \|\llbracket q_h \rrbracket\|_{0,\Gamma}^2 \\
&\geq C_u \|(\nabla + \mathbf{i}\mathbf{k})q_h\|_{0,\Omega_1 \cup \Omega_2}^2 - \frac{320}{\epsilon} \|W\|_{\infty} \|q_h\|_{1,\Omega_1 \cup \Omega_2}^2 + \frac{\lambda - 2\epsilon}{h} \|\llbracket q_h \rrbracket\|_{0,\Gamma}^2 \\
&\geq \frac{1}{2} C_u \|(\nabla + \mathbf{i}\mathbf{k})q_h\|_{0,\Omega_1 \cup \Omega_2}^2 + \frac{\lambda - 2\epsilon}{h} \|\llbracket q_h \rrbracket\|_{0,\Gamma}^2 + \\
& \quad \left(\frac{1}{2} C_u - \frac{320C_I}{\epsilon} \|W\|_{\infty} \right) \|(\nabla + \mathbf{i}\mathbf{k})q_h\|_{0,\Omega_1 \cup \Omega_2}^2.
\end{aligned}$$

Here, C_I is the constant such that $\|q_h\|_{1,\Omega_1 \cup \Omega_2} \leq C_I \|(\nabla + \mathbf{i}\mathbf{k})q_h\|_{0,\Omega_1 \cup \Omega_2}$ and we have used the fact $\|\mathbf{k}\| \leq 4$ in the first inequality. We conclude our proof of (3.26) by taking $\epsilon = 640\|W\|_{\infty} \frac{C_I}{C_u}$ and choosing the stability parameter $\lambda > 1280\|W\|_{\infty} \frac{C_I}{C_u}$. \square

Theorem 3.6 implies that the finite element eigenvalue value problem (3.15) is well-posed. According to the spectral theory, the discrete eigenvalue of (3.15) can be enumerated as

$$0 < E_h^1(\mathbf{k}) \leq E_h^2(\mathbf{k}) \leq \dots \leq E_h^{n_h}(\mathbf{k}) \quad (3.28)$$

and the corresponding L^2 -orthonormal eigenfunctions are $\phi_h^1, \phi_h^2, \dots, \phi_h^{n_h}$. Here, n_h is the dimension of the unfitted Nitsche's finite element space $V_{h,per}$, i.e. $n_h = \dim V_{h,per}$.

The key in the interpolation error estimations of the unfitted Nitsche's methods is to extend a function in the subdomain Ω_i to the whole domain Ω . For any $q \in H^2(\Omega_i)$, the extension operator of ϕ from $H^2(\Omega_i)$ to $H^2(\Omega)$ is denoted by X_i which satisfies

$$(X_i q)|_{\Omega_i} = q \quad (3.29)$$

and

$$\|X_i q\|_{s,\Omega} \leq C \|q\|_{s,\Omega_i}, \quad \text{for } s = 0, 1, 2. \quad (3.30)$$

Let $I_{i,h}$ be the standard nodal interpolation operator from $C(\overline{\Omega})$ to $V_{i,h}$. Define the interpolation operator for the finite element space V_h as

$$I_h^* q = (I_{1,h}^* q_1, I_{2,h}^* q_2), \quad (3.31)$$

where

$$I_{i,h}^* q = I_{i,h} X_i q_i, \quad i = 1, 2. \quad (3.32)$$

For the linear interpolation operator, [16] established the following optimal error estimates:

$$\|q - I_h^* q\|_{0,\Omega} + h \|q - I_h^* q\|_h \leq Ch^2 \|q\|_{2,\Omega_1 \cup \Omega_2}. \quad (3.33)$$

3.2. Unfitted Nitsche's method for computing edge modes. In this subsection, we generalize the unfitted Nitsche's method introduced in previous subsection to compute edge modes. Similarly, to model the wave propagation in the heterogeneous media, we will adopt the jump conditions. Let Γ_Σ be the union of interfaces in all cells in the fundamental domain of the cylinder. Based on this setup, edge states are the eigenpair of the following interface eigenvalue problem

$$\mathcal{L}^W \Psi(\mathbf{x}; k_\parallel) = E(k_\parallel) \Psi(\mathbf{x}; k_\parallel), \quad (3.34)$$

$$\Psi(\mathbf{x} + \mathbf{v}_1; k_\parallel) = e^{ik_\parallel} \Psi(\mathbf{x}; k_\parallel), \quad (3.35)$$

$$\Psi(\mathbf{x}; k_\parallel) \rightarrow 0 \quad \text{as } |\mathbf{x} \cdot \mathbf{k}_2| \rightarrow \infty, \quad (3.36)$$

$$[[\Psi]] = [[W \nabla \Psi \cdot \mathbf{n}]] = 0, \quad \text{on } \Gamma_\Sigma. \quad (3.37)$$

on the infinite domain Ω_Σ .

For the interface eigenvalue problem (3.34)–(3.42), the numerical challenges not only stem from the heterogeneity of the media and the quasi-periodicity of the boundary condition but also stem from the infinity nature of the cylindrical domain. For the second difficulty, thanks to the localization property of the eigenfunction in the \mathbf{v}_2 direction, we can truncate the infinite cylinder into a finite computational domain and replace the localization condition (3.36) by a homogeneous Dirichlet boundary condition. In specific, we define the truncated domain $\Omega_{\Sigma,L}$ as

$$\Omega_{\Sigma,L} \equiv \{\tau_1 \mathbf{v}_1 + \tau_2 \mathbf{v}_2 : 0 \leq \tau_1 \leq 1, -L \leq \tau_2 \leq L\}. \quad (3.38)$$

To handle the quasi-periodic boundary condition on \mathbf{v}_1 direction, we apply the Floquet-Bloch transformation $\Psi(\mathbf{x}; k_\parallel) = e^{i \frac{k_\parallel}{2\pi} \mathbf{k}_1 \cdot \mathbf{x}} \psi(\mathbf{x}; k_\parallel)$. Then, we reformulate the problem of finding edge states as computing the eigenpairs of the interface eigenvalue problem

$$\mathcal{L}^W(k_\parallel) \psi(\mathbf{x}; k_\parallel) = E(k_\parallel) \psi(\mathbf{x}; k_\parallel), \quad (3.39)$$

$$\psi(\mathbf{x} + \mathbf{v}_1; k_\parallel) = \psi(\mathbf{x}; k_\parallel), \quad (3.40)$$

$$\psi(\tau_1 \mathbf{v}_1 \pm L \mathbf{v}_2; k_\parallel) = 0, \quad \forall 0 \leq \tau_1 \leq 1, \quad (3.41)$$

$$[[\psi]] = [[W(\nabla + i\mathbf{k})\psi \cdot \mathbf{n}]] = 0, \quad \text{on } \Gamma_\Sigma. \quad (3.42)$$

where

$$\mathcal{L}^W(k_\parallel) = -(\nabla + i \frac{k_\parallel}{2\pi} \mathbf{k}_1) \cdot W(\nabla + i \frac{k_\parallel}{2\pi} \mathbf{k}_1). \quad (3.43)$$

3.2.1. Unfitted Nitsche's method in a cylinder. To present unfitted Nitsche's method on the truncated domain $\Omega_{\Sigma,L}$, we introduce the corresponding Sobolev spaces. Let $W^{k,p}(\Omega_{\Sigma,L})$ denote the Sobolev spaces of functions defined on $\Omega_{\Sigma,L}$ with norm $\|\cdot\|_{k,p}$ and seminorm $|\cdot|_{k,p}$. To incorporate the boundary conditions, we define

$$W_{per}^{k,p}(\Omega_{\Sigma,L}) \equiv \{\psi : \psi \in W^{k,p}(\Omega_{\Sigma,L}) \text{ and } \psi(\mathbf{x} + \mathbf{v}_1) = \psi(\mathbf{x})\}, \quad (3.44)$$

and

$$W_{per,0}^{k,p}(\Omega_{\Sigma,L}) \equiv \{\psi : \psi \in W_{per}^{k,p} \text{ and } \psi(\tau_1 \mathbf{v}_1 \pm L\mathbf{v}_2) = 0 \text{ for } 0 \leq \tau_1 \leq 1\}. \quad (3.45)$$

When $p = 2$, it is simply denoted as $H_{per}^k(\Omega_{\Sigma,L})$ or $H_{per,0}^k(\Omega_{\Sigma,L})$.

Note the fact that $\epsilon(\mathbf{x})$ is Λ -periodic. Then, the computational domain $\Omega_{\Sigma,L}$ can be split into two disjoint subdomains $\Omega_{\Sigma,L}^1$ and $\Omega_{\Sigma,L}^2$, where

$$\Omega_{\Sigma,L}^i = \Omega_{\Sigma,L} \cap (\Omega_i + \Lambda), \quad (3.46)$$

for $i = 1, 2$. The restriction of the interface Γ_{Σ} in $\Omega_{\Sigma,L}$ is denoted by $\Gamma_{\Sigma,L}$, i.e. $\Gamma_{\Sigma,L} = \Omega_{\Sigma,L}^1 \cap \Omega_{\Sigma,L}^2$. In Figure 3.2, we give a plot of the interface $\Gamma_{\Sigma,L}$ with $L = 10$.



Fig. 3.2: Plot of the interface $\Gamma_{\Sigma,L}$ with \mathbf{v}_2 being the x -axis and \mathbf{v}_1 being the y -axis.

Let $\hat{\mathcal{T}}_h$ denote the uniform triangular partition of the computational domain $\Omega_{\Sigma,L}$. The mesh $\hat{\mathcal{T}}_h$ is generated by firstly dividing $\Omega_{\Sigma,L}$ into $2LN^2$ sub-rhombuses with mesh size $h = \frac{\|\mathbf{v}_1\|}{N}$ and splitting each sub-rhombus into two triangles. Similarly, the elements in mesh $\hat{\mathcal{T}}_h$ can be classified as regular elements or interface elements. Let $\hat{\mathcal{T}}_{i,h}$ be the set all elements in $\hat{\mathcal{T}}_h$ covering the subdomain $\Omega_{\Sigma,L}^i$ for $i = 1, 2$. The union of all elements in $\hat{\mathcal{T}}_{i,h}$ is denoted by $\Omega_{\Sigma,L,h}^i$, which is defined as

$$\Omega_{\Sigma,L,h}^i = \bigcup_{K \in \mathcal{P}_{i,h}} K, \quad i = 1, 2. \quad (3.47)$$

As demonstrated in the previous section, $\Omega_{\Sigma,L,h}^1$ and $\Omega_{\Sigma,L,h}^2$ form an overlapping decomposition of the computational domain $\Omega_{\Sigma,L}$.

To introduce the finite element space for the unfitted Nitsche's method, we begin with defining the finite element space on each fictitious subdomain $\Omega_{\Sigma,L}^i$. Let $\hat{V}_{i,h}$ be the standard continuous finite element space on $\Omega_{\Sigma,h}^i$ which is defined as

$$\hat{V}_{i,h} = \left\{ v \in C^0(\Omega_{\Sigma,h}^i) : v|_K \in \mathbb{P}_1(K) \text{ for any } K \in \hat{\mathcal{T}}_{i,h} \right\}, \quad i = 1, 2. \quad (3.48)$$

Then, the unfitted Nitsche's finite element space \hat{V}_h is the direct sum of $\hat{V}_{1,h}$ and $\hat{V}_{2,h}$, i.e. $\hat{V}_h = \hat{V}_{1,h} \oplus \hat{V}_{2,h}$. To impose the periodic boundary condition in \mathbf{v}_1 direction and homogeneous Dirichlet boundary condition in \mathbf{v}_2 direction, we introduce the subspace $\hat{V}_{h,0} = \hat{V}_h \cap H_{per,0}^k(\Omega_{\Sigma,L})$.

Similar to the previous section, we define unfitted Nitsche's bilinear form $\hat{a}_h(\cdot, \cdot)$ as

$$\begin{aligned} \hat{a}_h(u_h, v_h) &= \sum_{i=1}^2 \int_{\Omega_{\Sigma, L}^i} W(\nabla + i \frac{k_{\parallel}}{2\pi} \mathbf{k}_1) u_h \cdot \overline{(\nabla + i \frac{k_{\parallel}}{2\pi} \mathbf{k}_1) v_h} dx - \\ &\quad \int_{\Gamma_{\Sigma, L}} \{W(\nabla + i \frac{k_{\parallel}}{2\pi} \mathbf{k}_1) u_h \cdot n\} \overline{[v_h]} ds - \\ &\quad \int_{\Gamma_{\Sigma, L}} \overline{\{W(\nabla + i \frac{k_{\parallel}}{2\pi} \mathbf{k}_1) v_h \cdot n\}} [u_h] ds + \\ &\quad \frac{\lambda}{h} \int_{\Gamma_{\Sigma, L}} [u_h] \overline{[v_h]} ds, \end{aligned}$$

Then, the unfitted Nitsche's method for the interface eigenvalue problem is to find the eigenpair $(\psi_h, E(k_{\parallel}))$ such that

$$\hat{a}_h(\psi_h, \eta_h) = E_h(k_{\parallel}) \hat{b}(\psi_h, \eta_h), \quad \forall \eta_h \in \hat{V}_{h,0}; \quad (3.49)$$

where

$$\hat{b}(\psi_h, \eta_h) = \int_{\Omega_{\Gamma}} \psi_h \cdot \overline{\eta_h} dx. \quad (3.50)$$

3.2.2. Well-posedness of unfitted Nitsche's method in a cylinder. Using the same argument as in previous subsection, we can prove the unfitted Nitsche's for is consistent in the following sense:

LEMMA 3.7. *Let $(\psi, E(k_{\parallel}))$ be the eigenpair of the interface eigenvalue problem (3.3)–(3.4). Then $(\psi, E(k_{\parallel})) \in H_{per,0}^1(\Omega_{\Sigma, L}) \times \mathbb{R}$ also satisfies*

$$\hat{a}_h(\psi, \eta) = E(k_{\parallel}) \hat{b}(\psi, \eta), \quad \forall \eta \in H_{per,0}^1(\Omega_{\Sigma, L}). \quad (3.51)$$

As a direct consequence of the above Lemma, we have the following Galerkin orthogonality:

COROLLARY 3.8. *Let $(\psi, E(k_{\parallel}))$ be the eigenpair of the interface eigenvalue problem (3.39)–(3.42) and $(\psi_h, E_h(k_{\parallel}))$ be the corresponding approximate eigenpair by the unfitted Nitsche's method. Then we have*

$$\hat{a}_h(\psi - \psi_h, \eta_h) = 0, \quad \forall \eta_h \in \hat{V}_{h,0}. \quad (3.52)$$

We also introduce the following energy norm

$$|||\psi|||_h^2 = \|(\nabla + i \frac{k_{\parallel}}{2\pi} \mathbf{k}_1) \psi\|_{0, \Omega_{\Sigma, L}^1 \cap \Omega_{\Sigma, L}^2}^2 + \sum_{K \in \hat{\mathcal{T}}_{\Gamma, h}} h^{-1} \|[\psi]\|_{0, \Gamma_K}^2. \quad (3.53)$$

In term of the energy norm, we shall show that the unfitted Nitsche's bilinear form is coercive and continuous in the following sense

THEOREM 3.9. *Suppose the stability parameter λ is large enough. Then there are exists two constants C_1 and C_2 such that*

$$C_1 |||q_h|||_h^2 \leq \hat{a}_h(q_h, q_h), \quad \forall q_h \in \hat{V}_h; \quad (3.54)$$

$$\hat{a}_h(q_h, \chi_h) \leq C_2 |||q_h|||_h |||\chi_h|||_h, \quad \forall q_h, \chi_h \in \hat{V}_{h,0}. \quad (3.55)$$

Theorem 3.9 also means the discrete eigenvalue value problem (3.15) is a well-posed problem. According to the spectral theory, the discrete eigenvalue of (3.15) can be enumerated as

$$0 < E_h^1(k_{\parallel}) \leq E_h^2(k_{\parallel}) \leq \cdots E_h^{n_h}(k_{\parallel}) \quad (3.56)$$

and the corresponding L^2 -orthonormal eigenfunctions are $\psi_h^1, \psi_h^2, \dots, \psi_h^{n_h}$. Here, n_h is the dimension of the unfitted Nitsche's finite element space $\hat{V}_{h,0}$.

Likewise, we use \hat{X}_i to denote the extension operator for functions defined $\Omega_{\Sigma,L}^i$ to $\Omega_{\Sigma,L}$ which satisfies

$$(\hat{X}_i \eta)|_{\Omega_i} = \eta \quad (3.57)$$

and

$$\|\hat{X}_i \eta\|_{s,\Omega} \leq C \|q\|_{s,\Omega_i}, \quad \text{for } s = 0, 1, 2. \quad (3.58)$$

Let $\hat{I}_{i,h}$ be the standard nodal interpolation operator from $C(\overline{\Omega_{\Sigma,L}})$ to $\hat{V}_{i,h}$. Define the interpolation operator for the finite element space \hat{V}_h as

$$\hat{I}_h^* q = (\hat{I}_{1,h}^* q_1, \hat{I}_{2,h}^* q_2), \quad (3.59)$$

where

$$\hat{I}_{i,h}^* q = \hat{I}_{i,h} \hat{X}_i q_i, \quad i = 1, 2. \quad (3.60)$$

We can also show the following interpolation error estimates:

$$\|\eta - \hat{I}_h^* \eta\|_{0,\Omega_{\Sigma,L}} + h \|\eta - \hat{I}_h^* \eta\|_h \leq Ch^2 \|\eta\|_{2,\Omega_{\Sigma,L}^1 \cup \Omega_{\Sigma,L}^2}. \quad (3.61)$$

4. Error analysis. In this section, we present unified error estimation for the proposed unfitted Nitsche's methods. Our main analysis tool is the Babuska-Osborn spectral approximation theory [5].

When we consider the eigenvalue problem (3.3)–(3.4), let $A_h(\cdot, \cdot)$ denote the Nitsche's bilinear function $a_h(\cdot, \cdot)$ which is defined on $V_A := H_{per}^1(\Omega)$ and $B_h(\cdot, \cdot)$ corresponding the L^2 inner production $b_h(\cdot, \cdot)$ on $V_B := L_{per}^2(\Omega)$. Similarly, when we consider the eigenvalue problem (3.39)–(3.42), let $A_h(\cdot, \cdot)$ denote the Nitsche's bilinear function $\hat{a}_h(\cdot, \cdot)$ which is defined on $V_a := H_{per,0}^1(\Omega_{\Sigma,L})$ and $B_h(\cdot, \cdot)$ corresponding the L^2 inner production $\hat{b}_h(\cdot, \cdot)$ on $V_b := L_{per}^2(\Omega_{\Sigma,L})$. The corresponding L^2 norm is denoted by $\|\cdot\|_b$. The Nitsche's finite element function is denoted by S_h which is either $V_{h,per}$ or $\hat{V}_{h,0}$.

For any $f \in V_b$, let $T : V_b \rightarrow V_a$ be the solution operator for the source problem such that

$$A_h(Tf, g) = (f, g), \quad \forall g \in V_a \quad (4.1)$$

We rewrite the interface eigenvalue problem (3.3)–(3.4) (or (3.39)–(3.42)) as

$$T\phi = \mu\phi \quad (4.2)$$

where $\mu = E(\mathbf{k})^{-1}$ (or $\mu = E(k_{\parallel})^{-1}$). For the source problem (4.1), we can show the following regularity [4, 19]

$$\|Tf\|_{2,*} \leq C \|f\|_b; \quad (4.3)$$

where the notation $\|\cdot\|_{2,\star}$ denotes the piecewise H^2 norm $\|\cdot\|_{2,\Omega_1\cup\Omega_2}$ or $\|\cdot\|_{2,\Omega_\Sigma^1\cup\Omega_\Sigma^2}$.

Similarly, we introduce the solution operator T_h for the discrete source problems which is defined as

$$a_h(T_h f, g_h) = (f, g_h), \quad \forall g_h \in S_h. \quad (4.4)$$

The unfitted Nitsche's method (3.15) has the following equivalent representation

$$T_h \phi_h = \mu_h \phi_h, \quad (4.5)$$

where $\mu_h = E_h(\mathbf{k})^{-1}$ (or $\mu_h = E_h(k_\parallel)^{-1}$). Evidently, both T and T_h are self-adjoint, elliptic, and compact linear operators.

Based on the interpolation error estimate, we can show the following error estimates for unfitted Nitsche's method approximating the source problem:

THEOREM 4.1. *Let T and T_h be the solution operators defined in (4.1) and (4.4), respectively. Then we have the following error estimates, for any $f \in L^2(\Omega)$,*

$$\|Tf - T_h f\|_h \leq Ch \|f\|_b, \quad (4.6)$$

$$\|Tf - T_h f\|_b \leq Ch^2 \|f\|_b. \quad (4.7)$$

Proof. The inequality (4.6) follows directly from Theorem 3.6 (or Theorem 3.9), the interpolation error estimate (3.33) (or (3.61)), and the regularity (4.3). The inequality (4.7) can be proved via the Aubin-Nitsche's tricks, see for example, [16]. \square

From the above theorem, we can deduce the following the corollary

COROLLARY 4.2. *Let T and T_h be the solution operator defined in (4.1) and (4.4), respectively. We have*

$$\|T - T_h\|_{\mathcal{L}(V_b)} \leq Ch^2. \quad (4.8)$$

Following the corollary, it is easily to show the following result

$$\lim_{h \rightarrow 0} \|T - T_h\|_{\mathcal{L}(V_b)} = 0. \quad (4.9)$$

Let $\rho(T)$ (or $\rho(T_h)$) denote the resolvent set of operator T (or T_h), and $\sigma(T)$ (or $\sigma(T_h)$) denote the spectrum set of operator T (or T_h). Using the above approximation property, we have the following property of no pollution of the spectrum which is a direct application of Theorem 9.1 in [6]

THEOREM 4.3. *For any compact set $K \subset \rho(T)$, there exist $h_0 > 0$ such that for all $h < h_0$, we have $K \subset \rho(T_h)$. If E is a nonzero eigenvalue of T with algebraic multiplicity equal to m , then there are m eigenvalues $E_h^1, E_h^1, \dots, E_h^m$ of T_h such that each E_h^m converges to E as h tends to 0.*

Suppose that $E \in \sigma(T)$ is a non-zero eigenvalue with algebraic multiplicity m . Theorem 4.3 implies that there are exactly m discrete eigenvalue of T_h converging to E as h tends to zero. For any closed smooth curve $\mathcal{C} \subset \rho(T)$ enclosing $E(\mathbf{k}) \in \sigma(T)$ and no other element of $\sigma(T)$, the Reisz spectral projection associated with $E(\mathbf{k})$ is defined as [5]

$$P = \frac{1}{2\pi i} \int_{\mathcal{C}} (z - T)^{-1} dz. \quad (4.10)$$

When h is sufficiently small, $\mathcal{C} \subset \rho(T_h)$ encloses exactly m discrete eigenvalues of T_h . We define analogously the discrete spectral projection

$$P_h = \frac{1}{2\pi i} \int_{\mathcal{C}} (z - T_h)^{-1} dz. \quad (4.11)$$

Now, we are ready to show our main eigenpair approximation results.

THEOREM 4.4. *Let μ_h be an eigenvalue of T_h such that $\lim_{h \rightarrow 0} \mu_h = \mu$. Let g_h be a unit eigenvector of T_h corresponding to the eigenvalue μ_h . Then there exists a unit eigenvector $g \in R(P)$ such that there following*

$$\|g - g_h\|_{0,\Omega} \leq Ch^2 \|g\|_{2,\star}, \quad (4.12)$$

$$|\mu - \mu_h| \leq Ch^2 \|g\|_{2,\star}, \quad (4.13)$$

$$|E - E_h| \leq Ch^2 \|g\|_{2,\star}. \quad (4.14)$$

Proof. We begin the first proof of the estimate (4.12). To do this, by applying the Theorem 7.4 in [5] and the operator approximation result (4.7), we can deduce that

$$\|g - g_h\|_{0,\Omega} \leq \|(T - T_h)|_{R(P)}\|_b = \sup_{\substack{q \in R(P) \\ \|q\|_a=1}} \|Tq - T_h q\|_{0,\Omega} \leq Ch^2 \|\phi\|_{2,\star},$$

which completes the proof of (4.12).

Then, we turn to the proof of the estimate (4.13). Let v_1, \dots, v_m be any basis for $R(P)$. Then, Theorem 7.3 in [5] implies that there exists a constant C such that

$$|\mu - \mu_h| \leq C \sum_{j,k=1}^m |((T - T_h)v_j, v_k)| + C \|(T - T_h)|_{R(P)}\|_{0,\Omega}^2. \quad (4.15)$$

To establish upper bound for $|\mu - \mu_h|$, it is sufficient to bound the first term in (4.15). Using (4.1), (4.4) and the Galerkin orthogonality (3.19) (or (3.52)), we have

$$\begin{aligned} ((T - T_h)v_j, v_k) &= (v_j, (T - T_h)v_k) \\ &= a_h(Tv_j, Tv_k - T_h v_k) \\ &= a_h(Tv_j - T_h v_j, Tv_k - T_h v_k) + a_h(T_h v_j, Tv_k - T_h v_k) \\ &= a_h(Tv_j - T_h v_j, Tv_k - T_h v_k) + \overline{a_h(Tv_k - T_h v_k, T_h v_j)} \\ &= a_h(Tv_j - T_h v_j, Tv_k - T_h v_k) \\ &\leq C \|Tv_j - T_h v_j\|_h \|Tv_k - T_h v_k\|_h \\ &\leq Ch^2 \|v_j\|_{2,\star} \|v_k\|_{2,\star} \\ &\leq Ch^2 \|g\|_{2,\star}^2. \end{aligned} \quad (4.16)$$

Notice the relationship between μ (or μ_h) and E (or E_h). Then, (4.14) is direct implication of (4.13). \square

5. Numerical Examples. In this section, we present a series of benchmark numerical examples to verify and validate our theoretical results and demonstrate that the proposed unfitted Nitsche's method is effective and efficient numerical methods to compute dispersive relation and edge modes for topological materials with high contrast material weights.

5.1. Numerical examples for computing dispersive relation. In this subsection, we numerically investigate the performance of the unfitted Nitsche's method for computing the dispersive relation. The material weight W is given in (2.8) with

$$\epsilon(\mathbf{x}) = \begin{cases} 1 + J, & \text{if } \mathbf{x} \in \Omega_1, \\ 1, & \text{if } \mathbf{x} \in \Omega_2. \end{cases}$$

The jump ratio of the material coefficient is $(1 + J)^2$. For large J , we have high contrast material weight. The radius of $B_r(\mathbf{A})$ and $B_r(\mathbf{B})$ is chosen to be 0.2.

5.1.1. Verification of Accuracy. In this part, we run a series a test to test the optimal convergence of the numerical eigenvalue obtained by the unfitted Nitsche's method. To measure the errors, we introduce the following relative error of eigenvalues

$$e_i = \frac{|E_{i,h_j}(\mathbf{k}) - E_{i,h_{j+1}}(\mathbf{k})|}{E_{i,h_{j+1}}(\mathbf{k})}.$$

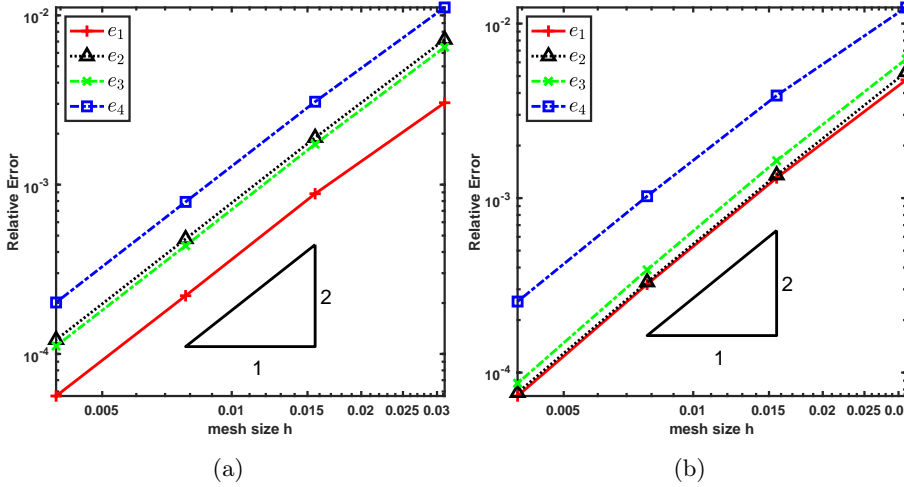


Fig. 5.1: Numerical errors for eigenvalue approximation : (a) $J = 2$ and $\gamma = 0$; (b) $J = 2$ and $\gamma = 0.1$.

We test the numerical methods with different choices of J and γ . The numerical errors of the first four eigenvalues are plotted in Figs 5.1–5.2, where the numerical eigenvalues converge at the optimal rate $\mathcal{O}(h^2)$. This confirms that the error estimate for the unfitted Nitsche's method is uniform with respect to the jump ratio of $(J+1)^2$.

5.1.2. Numerical investigation of the dispersive relation. In this part, we try to compute the dispersive relation and make some comparison with the Fourier spectral methods [21, 34], which uses the Fourier modes as basis functions. For the unfitted Nitsche's method, we use the meshes with mesh size $h = \frac{1}{64}$. For the Fourier spectral method, we use 16 Fourier modes in each direction.

We consider the case with a relative larger jump ratio with $J = 30$. We show the numerical results in Figure 5.3. For the unfitted Nitsche's method, we can still observe the existence of the Dirac point for $\gamma = 0$ and the disappearance of the Dirac point when $\gamma = 0.1$. But the Fourier spectral method seems to fail to give the correct numerical results in the case. In specific, we can see the gap between the first eigencurve and the second eigencurve opens up when $\gamma = 0$ and the eigencurves are not symmetric. The performance is not improved even when we increase the number of Fourier modes in each direction. From those two figures, we can clearly see the incorrectness of the Fourier spectral methods. However, we can observe the same mechanism of the Dirac point for unfitted Nitsche's method.

(a) (b)

Fig. 5.2: Numerical errors for eigenvalue approximation : (a) $J = 100$ and $\epsilon = 0$; (b) $J = 100$ and $\epsilon = 0.1$.

(a) (b) (c) (d)

Fig. 5.3: Dispersive relation when $J = 30$ (a) Un tted Nitsche's Method with $\epsilon = 0$; (b) Spectral Method with $\epsilon = 0$; (c) Un tted Nitsche's Method with $\epsilon = 0.1$; (d) Spectral Method with $\epsilon = 0.1$

To make a quantitative comparison of those two methods for the small jump ratio case, we graph the results of those two methods in the same plot when $h = 2$ in Figure 5.4. In the Figure, the numerical results generated by the un tted Nitsche's method are shown by solid curves and the numerical results generated by the Fourier spectral method are represented by dashed curves. We can see that the numerical eigenvalues given by the un tted Nitsche's method are lower than the counterpart given by the Fourier spectral methods. This observation implies that the un tted Nitsche's method is much more accurate than the Fourier spectral method since both methods are Galerkin methods which give upper bounds of the exact eigenvalues.

In summary, it has been seen from the above numerical results that the Fourier spectral method can only provide the correct numerical results for small jump ratios. In contrast, the un tted Nitsche's method can simulate the physical phenomena for arbitrary large jump ratio.

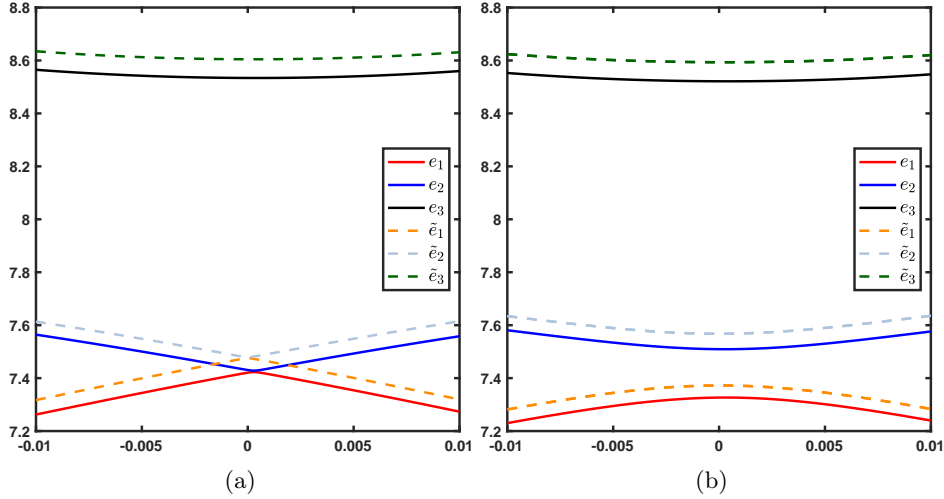


Fig. 5.4: Comparison of the unfitted Nitsche's method and the Fourier spectral method (solid line: the Unfitted Nitsche's method and dashed line: the Fourier spectral method) (a) $J = 2$ and $\gamma = 0$; (b) $J = 2$ and $\gamma = 0.1$

5.2. Numerical examples for computing edge modes. In this subsection, we present numerical examples to show the unfitted Nitsche's method proposed in Section 4 is an efficient numerical method for computing topologically protected edge modes with high contrast material weight and supports the theoretical result for eigenvalue approximation. In this subsection, we consider the material weight is given in the form

$$W(\mathbf{x}) = \epsilon(\mathbf{x})^{-1} + \delta\kappa(\delta\mathbf{k}_2 \cdot x)\epsilon(\mathbf{x})^{-2}\sigma_2. \quad (5.1)$$

where

$$\epsilon(\mathbf{x}) = \begin{cases} 1 + J, & \text{if } \mathbf{x} \in \Omega_1, \\ 1, & \text{if } \mathbf{x} \in \Omega_2. \end{cases}$$

In (5.1), δ is constant which determine the height of domain. It is chosen such that the coefficient matrix W is symmetric positive definite. The function $\kappa(\cdot)$ is the domain wall function in (2.11).

5.2.1. Verification of Accuracy. In this section, we conduct a benchmark numerical study to verify the optimal convergence of the unfitted Nitsche's method (3.49). Similarly, the convergence rate is approximated by the following the relative errors

$$\hat{e}_i = \frac{|E_{i,h_j}(k_{\parallel}) - E_{i,h_{j+1}}(k_{\parallel})|}{E_{i,h_{j+1}}(k_{\parallel})}.$$

In this test, we take $k_{\parallel} = 0.56\pi$, $\delta = 0.1$ and $L = 10$. We focus on the computation of the first six eigenvalues. The numerical results of the convergence test are summarized in Figure 5.5 for $J = 2$ and $J = 10$. From the data in Figure 5.5, it is apparent that the numerical eigenvalues computed using the unfitted Nitsche's method

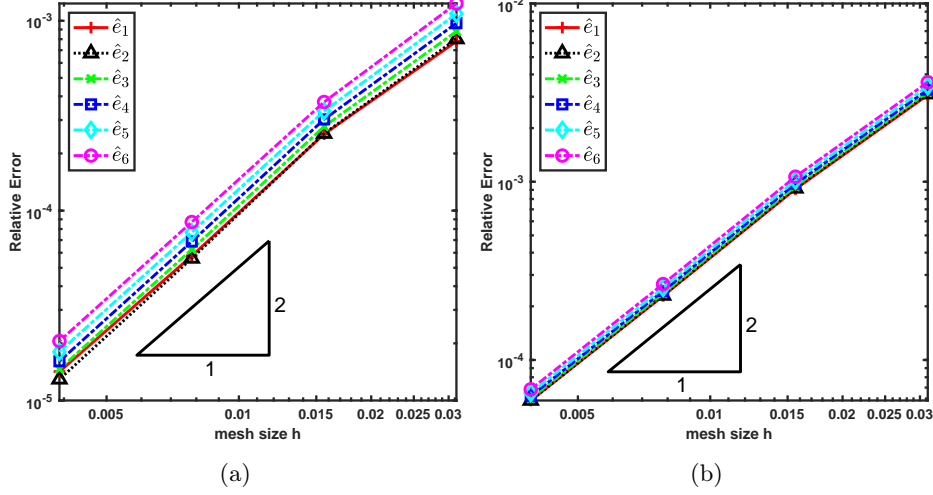


Fig. 5.5: Numerical errors for eigenvalue approximation : (a) $J = 2$ and $\delta = 0.1$; (b) $J = 10$ and $\delta = 0.1$.

(3.49) converges at the optimal rate $\mathcal{O}(h^2)$. It is consistent with the theoretical result in the Theorem 4.4.

5.2.2. Computation of the topological edge modes. In this paper, we provide numerical examples to demonstrate that the proposed unfitted Nitsche's method is an efficient method to compute the topological edge modes in the heterogeneous setting.

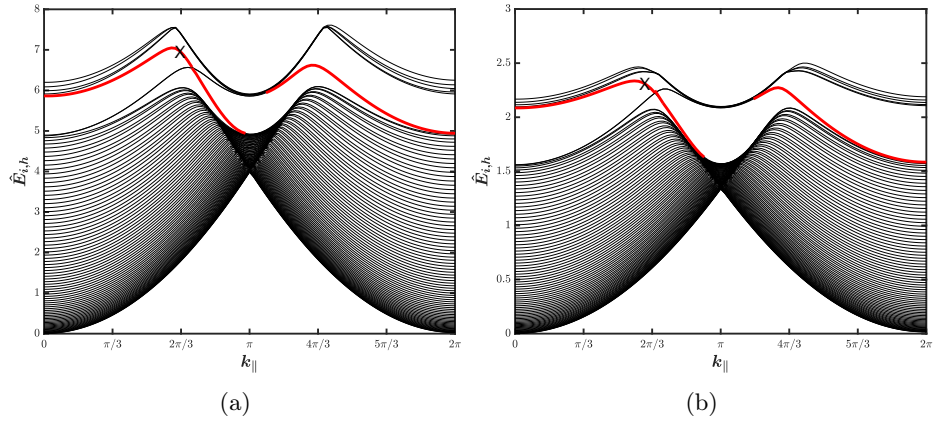


Fig. 5.6: Plot of the first 85 eigencurves for with $L = 80$ where the edge mode is corresponding to the line mark by 'X': (a) Case $J = 2$ and $\delta = 0.6$; (b) Case $J = 10$ and $\delta = 0.7$.

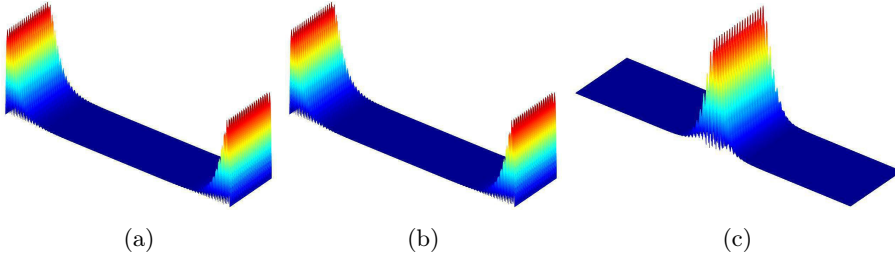


Fig. 5.7: Plot of the module of the eigenfunctions: (a) The 79th eigenfunction; The 80th eigenfunction; (c) The 81th eigenfunction

Test case 1. First of all, we consider the computation of the topological edge states with small jump ratio. In this test, we choose $J = 2$, $\delta = 0.6$ and $L = 80$. In Figure 5.6a, we show the plot of first 85 eigencurves in term of k_{\parallel} . In Figure 5.6a, we can see that the red eigencurve is separated from the eigencurves, which indicates edge states. To demonstrate the existence of edge states, we sketch the module of the 79th, 80th, and 81th eigenfunctions at the point $k_{\parallel} = \frac{2\pi}{3}$ in Figure 5.7. What stands out in the table is that the 81th eigenfunction is located at the center of the computational domain but the 79th and 80th are both located the boundary of the computational domain. It suggests that the 81th eigenpair is the edge state. The other two are referred as pseudo edge state which occur due the artificial truncation of the computational domain.

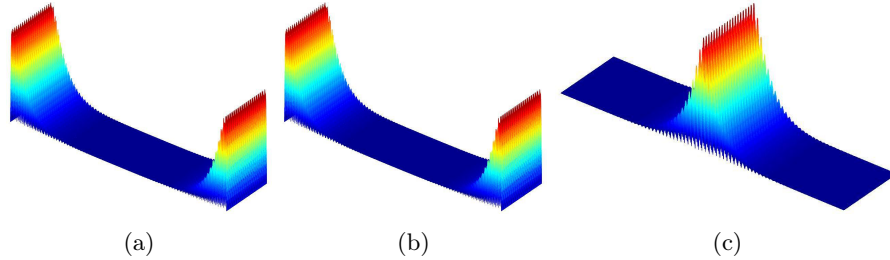


Fig. 5.8: Plot of the module of the eigenfunctions: (a) The 79th eigenfunction; The 80th eigenfunction; (c) The 81th eigenfunction

Test case 2. Then, we consider a relative large jump ratio. In this test, we choose $J = 10$, $\delta = 0.7$ and $L = 80$. The plot of eigencurves are presented In Figure 5.6b. Similarly, we also show the plot of the module of the 79th, 80th, and 81th eigenfunctions at the point $k_{\parallel} = \frac{2\pi}{3}$ in Figure 5.8. We observe the same phenomena as in **Test case 1**. In particular, we can observe the existence of edge mode.

6. Conclusion. In this paper, we propose new unfitted Nitsche's methods based on the Floquet-Bloch transform for efficiently simulating photonic graphene with heterogeneous structure. By taking advantage of the structure of underlying meshes, we establish a sharp trace inequality for cut element, which is the key ingredient to show

the stability of the Nitsche's bilinear forms. The theoretical foundation of the proposed methods builds upon the abstract spectral approximation theory by Babuška and Osborn. The performance of the proposed unfitted methods is tested using a series of benchmark numerical examples. Numerical comparison with the Fourier spectral method is also presented. In future, we plan to combine the superconvergent tool for unfitted Nitsche's method in [12] to further improve the accuracy and reduce the CPU time.

Acknowledgment. The authors thank Professor Michael I. Weinstein for useful discussions. H.G. was partially supported by Andrew Sisson Fund of the University of Melbourne, X.Y. was partially supported by the NSF grant DMS-1818592, and Y.Z. was partially supported by NSFC grant 11871299.

Appendix A. Proof of the Lemma 3.4.

A.1. A technique Lemma. Before we give a proof of the Lemma 3.4, we present a lemma that we shall use.

LEMMA A.1. *Let $\mathbf{x}^j = (x_1^j, x_2^j)$, for $j = 1, 2, 3$, be the three vertices triangle K and $b_i(\mathbf{x})$ be the standard nodal basis function associated with \mathbf{x}^j . Then the following relationship holds*

$$|b_j(\mathbf{x})| \leq 4h|\nabla b_j| \quad (\text{A.1})$$

for $j = 1, 2, 3$.

Proof. Without loss of generality, we only prove (A.1) for $i = 1$. Using the area coordinates [9], we have

$$b_1(\mathbf{x}) = \frac{(x_2 - x_2^3)(x_1^3 - x_1^2) - (x_1 - x_1^2)(x_2^3 - x_2^2)}{2|K|}, \quad (\text{A.2})$$

and

$$\nabla b_i = \left(\frac{-(x_2^3 - x_2^2)}{2|K|}, \frac{(x_1^3 - x_1^2)}{2|K|} \right). \quad (\text{A.3})$$

From the above two expressions, we can deduce that

$$|b_i(\mathbf{x})| \leq 2h \frac{|x_1^3 - x_1^2| + |(x_2^3 - x_2^2)|}{2|K|} \leq 4h \frac{\sqrt{|x_1^3 - x_1^2|^2 + |(x_2^3 - x_2^2)|^2}}{2|K|} = 4h|\nabla b_i|$$

where we have used the fact the triangle K is an isosceles triangle which implies $\text{diam}(K) \leq 2h$. \square

A.2. Proof of Lemma 3.4. *Proof.* It is sufficient to show the lemma for the basis functions b_j since ϕ_h is a linear combination of b_j . Using Lemma A.1, we can deduce that

$$\|b_j\|_{0,\Gamma_T}^2 \leq |\Gamma_T| \|b_j\|_{0,\infty,\Gamma_T}^2 \leq |\Gamma_T| \|b_j\|_{0,\infty,K_i}^2 \leq 4h|\Gamma_T| |\nabla b_i| = \frac{4h|\Gamma_T|}{|K_i|} \|\nabla b_i\|_{0,K_i}^2;$$

which completes our proof of (3.21). The inequality (3.22) is implied in the above proof. \square

REFERENCES

- [1] M J ABLOWITZ, S D NIXON, AND Y ZHU, *Conical diffraction in honeycomb lattices*, Physical Review A, 79 (2009), p. 053830.
- [2] M. J. ABLOWITZ AND Y. ZHU, *Nonlinear waves in shallow honeycomb lattices*, SIAM J. Appl. Math., 72 (2012), pp. 240–260.
- [3] C. ANNAVARAPU, M. HAUTEFEUILLE, AND J. E. DOLBOW, *A robust Nitsche’s formulation for interface problems*, Comput. Methods Appl. Mech. Engrg., 225/228 (2012), pp. 44–54.
- [4] I. BABUŠKA, *The finite element method for elliptic equations with discontinuous coefficients*, Computing (Arch. Elektron. Rechnen), 5 (1970), pp. 207–213.
- [5] I. BABUŠKA AND J. OSBORN, *Eigenvalue problems*, in Handbook of numerical analysis, Vol. II, Handb. Numer. Anal., II, North-Holland, Amsterdam, 1991, pp. 641–787.
- [6] D. BOFFI, *Finite element approximation of eigenvalue problems*, Acta Numer., 19 (2010), pp. 1–120.
- [7] E. BURMAN, S. CLAUS, P. HANSBO, M. G. LARSON, AND A. MASSING, *CutFEM: discretizing geometry and partial differential equations*, Internat. J. Numer. Methods Engrg., 104 (2015), pp. 472–501.
- [8] Z. CHEN AND J. ZOU, *Finite element methods and their convergence for elliptic and parabolic interface problems*, Numer. Math., 79 (1998), pp. 175–202.
- [9] P. G. CIARLET, *The finite element method for elliptic problems*, vol. 40 of Classics in Applied Mathematics, Society for Industrial and Applied Mathematics (SIAM), Philadelphia, PA, 2002. Reprint of the 1978 original [North-Holland, Amsterdam; MR0520174 (58 #25001)].
- [10] H. GUO AND X. YANG, *Gradient recovery for elliptic interface problem: II. Immersed finite element methods*, J. Comput. Phys., 338 (2017), pp. 606–619.
- [11] ———, *Gradient recovery for elliptic interface problem: I. Body-fitted mesh*, Commun. Comput. Phys., 23 (2018), pp. 1488–1511.
- [12] ———, *Gradient recovery for elliptic interface problem: III. Nitsche’s method*, J. Comput. Phys., 356 (2018), pp. 46–63.
- [13] H. GUO, X. YANG, AND Z. ZHANG, *Superconvergence of partially penalized immersed finite element methods*, IMA J. Numer. Anal., 38 (2018), pp. 2123–2144.
- [14] H. GUO, X. YANG, AND Y. ZHU, *Bloch theory-based gradient recovery method for computing topological edge modes in photonic graphene*, J. Comput. Phys., 379 (2019), pp. 403–420.
- [15] F D M HALDANE AND S RAGHU, *Possible realization of directional optical waveguides in photonic crystals with broken time-reversal symmetry*, Physical review letters, 100 (2008), p. 013904.
- [16] A. HANSBO AND P. HANSBO, *An unfitted finite element method, based on Nitsche’s method, for elliptic interface problems*, Comput. Methods Appl. Mech. Engrg., 191 (2002), pp. 5537–5552.
- [17] S. HOU AND X.-D. LIU, *A numerical method for solving variable coefficient elliptic equation with interfaces*, J. Comput. Phys., 202 (2005), pp. 411–445.
- [18] S. HOU, P. SONG, L. WANG, AND H. ZHAO, *A weak formulation for solving elliptic interface problems without body fitted grid*, J. Comput. Phys., 249 (2013), pp. 80–95.
- [19] R. B. KELLOGG, *On the Poisson equation with intersecting interfaces*, Applicable Anal., 4 (1974/75), pp. 101–129. Collection of articles dedicated to Nikolai Ivanovich Muskhelishvili.
- [20] A. B. KHANIKAEV, S. H. MOUSAVI, W.-K. TSE, M. KARGARIAN, A. H. MACDONALD, AND G. SHVETS, *Photonic topological insulators*, Nature materials, 12 (2013), pp. 233–239.
- [21] J. P. LEE-THORP, M. I. WEINSTEIN, AND Y. ZHU, *Elliptic operators with honeycomb symmetry: Dirac points, edge states and applications to photonic graphene*, Arch. Ration. Mech. Anal., 232 (2019), pp. 1–63.
- [22] R. J. LEVEQUE AND Z. LI, *The immersed interface method for elliptic equations with discontinuous coefficients and singular sources*, SIAM J. Numer. Anal., 31 (1994), pp. 1019–1044.
- [23] Z. LI, *The immersed interface method using a finite element formulation*, Appl. Numer. Math., 27 (1998), pp. 253–267.
- [24] Z. LI AND K. ITO, *The immersed interface method*, vol. 33 of Frontiers in Applied Mathematics, Society for Industrial and Applied Mathematics (SIAM), Philadelphia, PA, 2006. Numerical solutions of PDEs involving interfaces and irregular domains.
- [25] Z. LI, T. LIN, AND X. WU, *New Cartesian grid methods for interface problems using the finite element formulation*, Numer. Math., 96 (2003), pp. 61–98.
- [26] T. LIN, Y. LIN, AND X. ZHANG, *Partially penalized immersed finite element methods for elliptic interface problems*, SIAM J. Numer. Anal., 53 (2015), pp. 1121–1144.
- [27] L LU, J D JOANNOPOULOS, AND M SOLJAČIĆ, *Topological photonics*, Nature Photonics, 8 (2014), pp. 821–829.
- [28] S H MOUSAVI, A B KHANIKAEV, AND Z WANG, *Topologically protected elastic waves in phononic metamaterials*, Nature communications, 6 (2015).

- [29] J. NITSCHKE, *über ein Variationsprinzip zur Lösung von Dirichlet-Problemen bei Verwendung von Teilräumen, die keinen Randbedingungen unterworfen sind*, Abh. Math. Sem. Univ. Hamburg, 36 (1971), pp. 9–15. Collection of articles dedicated to Lothar Collatz on his sixtieth birthday.
- [30] C. S. PESKIN, *Numerical analysis of blood flow in the heart*, J. Computational Phys., 25 (1977), pp. 220–252.
- [31] ———, *The immersed boundary method*, Acta Numer., 11 (2002), pp. 479–517.
- [32] Y PLOTNIK, M C RECHTSMAN, D SONG, M HEINRICH, J M ZEUNER, S NOLTE, Y LUMER, N MALKOVA, J XU, A SZAMEIT, Z CHEN, AND M SEGEV, *Observation of unconventional edge states in ‘photonic graphene’*, Nature materials, 13 (2014), pp. 57–62.
- [33] M C RECHTSMAN, J M ZEUNER, Y PLOTNIK, Y LUMER, D PODOLSKY, F DREISOW, S NOLTE, M SEGEV, AND A SZAMEIT, *Photonic floquet topological insulators*, Nature, 496 (2013), pp. 196–200.
- [34] MAKSIM SKOROBOGATIY AND JIANKE YANG, *Fundamentals of photonic crystal guiding*, Cambridge University Press, 2009.
- [35] R SÜSSTRUNK AND S D HUBER, *Observation of phononic helical edge states in a mechanical ‘topological insulator’*, Science, 349 (2015), pp. 47–50.
- [36] LLOYD N. TREFETHEN, *Spectral methods in MATLAB*, SIAM, 2000.
- [37] L. WANG, H. ZHENG, X. LU, AND L. SHI, *A Petrov-Galerkin finite element interface method for interface problems with Bloch-periodic boundary conditions and its application in phononic crystals*, J. Comput. Phys., 393 (2019), pp. 117–138.
- [38] M XIAO, G MA, Z YANG, P SHENG, Z Q ZHANG, AND C T CHAN, *Geometric phase and band inversion in periodic acoustic systems*, Nature Physics, 11 (2015), pp. 240–244.